Analysis and Suppression of Induced Circulating Currents in Segmented DWPT Systems With a Primary-Side LCC Compensation Network

Yongping Yin, Guangyao Li, *Member, IEEE*, Xin Gao, *Member, IEEE*, Chang Liu, Shuai Dong, and Chunbo Zhu

***Abstract*—In segmented dynamic wireless power transfer (DWPT) systems, the presence of cross-coupling mutual inductance leads to the generation of induced circulating current (ICC) in the inactive rails, resulting in power loss, magnetic field leakage, increased inverter capacity, and reduced efficiency. To address this problem, a parameter configuration method based on resonance tuning coefficient λ is proposed. This method effectively suppresses ICC, reduces inverter capacity, and improves system efficiency. In addition, it is found that the abnormal drop in inverter current during λ tuning is caused by multiple resonance points at the inverter input impedance. For scenarios involving multiple power supply rails (PSRs), it is revealed that under conventional parameter configuration method, the ICC exhibits hyperbolic-sine-type damped diffusion behavior. Building on this, a general circuit analysis model is proposed for different operating modes of PSR, with circuit parameters summarized and a design flowchart provided. Finally, a 12-meter DWPT platform is built to validate the proposed method, achieving maximum output power of 63.39 kW and system efficiency of 94.15%.**

***Index Terms*—Cross-coupling, dynamic wireless power transfer (DWPT), induced circulating current (ICC) suppression, multiple resonant points, segmented rails.**

Nomenclature

MI	Mutual inductance.
ICC	Induced circulating current.
IAR	Inactive rail.
AR	Active rail.
PSR	Power supply rail.
CPCM	Conventional parameter configuration method.
PPCM	Proposed parameter configuration method.
λ	Resonance tuning coefficient.

Received 30 September 2025; revised 6 December 2025; accepted 27 December 2025. Date of publication 5 January 2026; date of current version 20 March 2026. This work was supported by the National Natural Science Foundation of China under Grant 52177003. Recommended for publication by Associate Editor M. Ponce-Silva. *(Corresponding author: Guangyao Li.)*

Yongping Yin, Xin Gao, Chang Liu, Shuai Dong, and Chunbo Zhu are with the School of Electrical Engineering and Automation, Harbin Institute of Technology, Harbin 150001, China, and also with the Zhengzhou Research Institute, Harbin Institute of Technology, Zhengzhou 450000, China (e-mail: yinyongping@hit.edu.cn; gaoxin@hit.edu.cn; 23b936188@stu.hit.edu.cn; dongshuai@hit.edu.cn; zhuchunbo@hit.edu.cn).

Guangyao Li is with the Zhengzhou Research Institute, Harbin Institute of Technology, Zhengzhou 450000, China (e-mail: liguangyao@hitzri.cn).

Color versions of one or more figures in this article are available at https://doi.org/10.1109/TPEL.2025.3650608.

Digital Object Identifier 10.1109/TPEL.2025.3650608

I. Introduction

As a novel energy transfer method, dynamic wireless power transfer (DWPT) has attracted significant attention in recent years [1], [2]. Compared with traditional wired charging, DWPT can greatly extend driving range, reduce maintenance costs, and enhance system safety and environmental adaptability. Therefore, it has been widely studied in electric vehicles, inspection robots, and rail transportation [3], [4], [5].

In DWPT systems, PSRs are generally divided into two types: long rails [6], [7] and segmented rails [8], [9], [10]. The former has a simple structure and ensures continuous power delivery during receiver movement without power fluctuation. However, long rails suffer from large parasitic resistance, resulting in low system efficiency and serious magnetic field leakage [11]. In contrast, segmented PSRs can be selectively activated based on the position of the receiver, which significantly improves efficiency and reduces magnetic field leakage.

In segmented PSR systems, rail spacing is a key factor affecting system performance. If the spacing is too large, the MI between PSR and receiver drops significantly during transitions, leading to large power fluctuations and reduced stability of power delivery [5], [12]. Reducing the spacing helps maintain stable MI and suppress power fluctuations in the transition zone, but it introduces cross-coupling MI between adjacent rails [9], [13]. Under this effect, an induced voltage is generated on the IAR due to the current in the active rail (AR). In low-power or weak cross-coupling systems, the induced voltage is small and can be ignored. However, in high-power systems, the current in the AR is usually large [14], [15], which may cause significant induced voltage in the adjacent IAR loop, generating large ICC. This results in increased magnetic leakage and power loss, and may even pose risks to circuit components and disturb system operation.

Cross-coupling MI not only causes ICC but also affects the resonance status of circuits [16], [17]. Most existing studies focus on mitigating its impact on resonance, while little attention has been paid to suppressing the ICC. Based on existing studies on mitigating the cross-coupling MI, methods for suppressing ICC can be categorized into two types. The first type inserts switching devices into each rail loop to disconnect IARs through control logic, thereby blocking the ICC path [9], [18]. The

second type designs decoupled PSR structures or introduces decoupling circuits to eliminate the cross-coupling MI effect.

Although inserting electrical switches can theoretically block the ICC, the switches may generate voltage spikes and electromagnetic interference, and a complex control system is also required. In systems with multiple segmented rails, the complexity and cost increase significantly, and reliability becomes a challenge.

Structural decoupling of PSRs can be achieved by simply coil overlapping, forming a magnetic coupler similar to the bipolar coil in static WPT systems [6]. However, due to parameter asymmetries in practical systems, complete decoupling of PSRs is difficult to achieve; moreover, the overlapped area may cause significant power fluctuations at the receiver during transitions, affecting power stability [9]. In high-power applications, the overlapping region may also lead to increased local insulation stress and heat generation. In [10], [19], [20], and [21], bipolar and unipolar coil overlapping layouts were used to eliminate cross-coupling MI between PSRs. However, these methods increased the overall volume and weight of the rails and introduced similar insulation and thermal issues. In [22], a decoupling structure was achieved by placing a bipolar coil between two unipolar PSRs. However, this layout requires multiple rails to be energized simultaneously to ensure stable power delivery, which increases system cost in long-distance operating scenarios due to additional coils and frequent switching. Alternatively, decoupling transformers can be inserted between PSRs [23], [24]. However, in systems with multiple segmented rails, inserting decoupling transformers significantly increases the overall cost and power loss.

It can be seen that existing methods for suppressing ICC in long-distance and high-power DWPT systems often face challenges such as high cost and poor reliability. Therefore, a simple, reliable, and low-cost ICC suppression method is urgently needed. Meanwhile, in segmented PSR systems, the movement of the receiver changes the number of ARs and circuit parameters, resulting in multiple operating modes. However, studies on the cross-coupling effect and ICC distribution under different operating modes are still lacking, and no unified analytical model or engineering design guidelines are available.

To address the above-mentioned challenges, the characteristics of ICC and its suppression mechanism are investigated, and a parameter suppression scheme based on the resonance tuning coefficient λ is proposed in this article. The contributions are summarized as follows.

1) A suppression method for ICC based on the resonance tuning factor λ was proposed. The PPCM suppresses ICC, improves system efficiency, and reduces inverter current and capacity without increasing system cost or altering the output characteristics.
2) It was found that when the internal resistance of the PSR loop is small, the inverter input side exhibits multiple resonance points as the resonance tuning coefficient λ varies.
3) It was revealed that the ICC shows a hyperbolic-sine-type damped diffusion behavior in systems with multiple IARs when the CPCM is used.

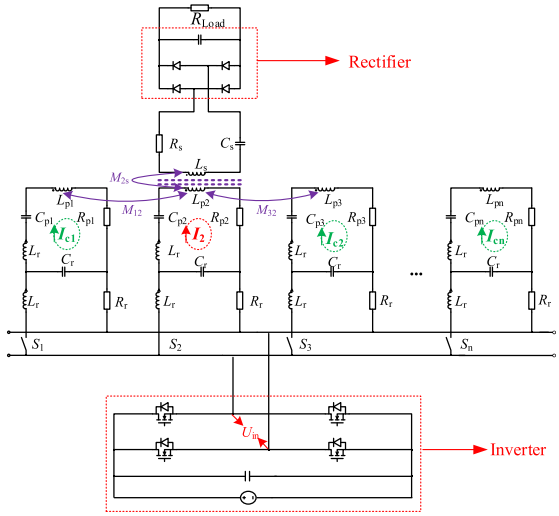

Fig. 1. Schematic circuit of DWPT system.

4) A general circuit analysis model for different PSR operating modes was developed. The model calculates ICC, inverter current, output power, and other circuit parameters quickly and accurately.

The rest of this article is organized as follows. Section II describes the system topology and PPCM, and Section III analyzes the performance of PPCM. Section IV presents the diffusion behavior of ICC together with the general circuit analysis model. Section V provides the experimental verification, and Section VI concludes this article.

II. Analysis of the ICC Characteristics Under the CPCM

The basic schematic circuit of the DWPT system used in this paper is shown in Fig. 1 [25]. The system comprises n PSRs, labeled L_{p1}, L_{p2}, …, L_{pn}, and a single receiver coil L_s. All PSRs share one inverter and are controlled by switches S_1-S_n. The LCC-S compensation network is adopted. In Fig. 1, L_{p2} is selected as the AR, while the others are IARs. For simplicity, only a single receiver is considered in this article. It is noted that the MI of the receiver changes continuously during the transition between two PSRs. Under series compensation for PSRs, a small MI results in low inverter input impedance and high inverter current [3], which may cause damage to the inverter. In contrast, under LCC compensation for PSRs, the inverter current increases proportionally with the MI [3]. Therefore, LCC compensation network is considered more suitable for PSRs in DWPT systems.

To ensure stable power delivery during receiver transitions, the spacing between adjacent PSRs is usually small [5], [9]. In this case, cross-coupling MI exists between adjacent PSRs, such as M_{12} and M_{32} in Fig. 1. In long-distance DWPT systems, the length of a single PSR is usually greater than 1 m [14], [15]. Under this condition, the cross-coupling MI between nonadjacent PSRs becomes very weak and is neglected in this article. The cross-coupling MI induces voltages in IARs, resulting in circulating currents, known as ICCs. Assuming the nth rail is

inactive, the ICC I_{cn} can be derived based on the MI model and Kirchhoff's law [26], as follows:

$$I_{cn} = \frac{-j\omega M_{(n-1)n} I_{n-1} - j\omega M_{(n+1)n} I_{n+1}}{X_{pn} + R_{pn}} \tag{1}$$

where $I_{n\text{-}1}$ and I_{n+1} are the currents in the PSRs adjacent to the nth rail on the left and right sides, respectively, and $M_{(n\text{-}1)\,n}$ and $M_{(n+1)\,n}$ are the MIs from the $(n-1)$th and $(n+1)$th rails to the nth rail, respectively. R_{pn} is the equivalent internal resistance of the nth PSR. X_{pn} is

$$X_{pn} = j\omega L_{pn} - j\frac{1}{\omega C_{pn}} \tag{2}$$

where ω is the operating angular frequency of the system.

To reduce reactive power and improve efficiency, the CPCM generally satisfies [27]

$$C_r = \frac{1}{\omega^2 L_r}, C_{pn} = \frac{1}{\omega^2 L_{pn}},\ C_s = \frac{1}{\omega^2 L_s}, n \in N^*. \tag{3}$$

In this case, the AR current I_p is independent of the load and is given by

$$I_p = \frac{U_{\text{in}}}{j\omega L_r} \tag{4}$$

where U_{in} is the fundamental component of the inverter output voltage.

Substituting (3) and (2) into (1) yields

$$I_{cn} = \frac{-j\omega M_{(n-1)n} I_{n-1} - j\omega M_{(n+1)n} I_{n+1}}{R_{pn}}. \tag{5}$$

By comparing (5) with (1), it can be seen that (5) represents the maximum value of (1), which means that the ICC reaches its highest value when the CPCM is used. In addition, it can be seen from (5) that the ICC increases as the current in the adjacent AR increases. In high-power applications, high AR currents may induce high ICCs in IARs, leading to power loss, reduced efficiency, increased inverter capacity, and severe magnetic field leakage. These drawbacks highlight the limitations of the CPCM and motivate the need for an effective suppression method. To address this issue, a novel parameter configuration method is proposed in the following section.

III. Proposed Method and Performance Analysis

A. Proposed Method

To reduce the ICC, the expression in (1) is first analyzed. In general, for a completed system design, the current and frequency of the AR are fixed, and the cross-coupling MI typically exists. Therefore, the numerator in (1) is difficult to adjust. In the denominator, the equivalent resistance R_{pn} and the self-inductance L_{pn} of the PSR are also difficult to modify. As a result, adjusting C_{pn} becomes a viable approach for achieving better system performance.

As described in Section II when the conventional method is used, C_p satisfies (3), at which point X_p becomes zero and the ICC reaches its maximum. When C_p does not satisfy (3), (1) and (2) show that the magnitude of X_p increases, and the magnitude of the ICC decreases. For a system with multiple

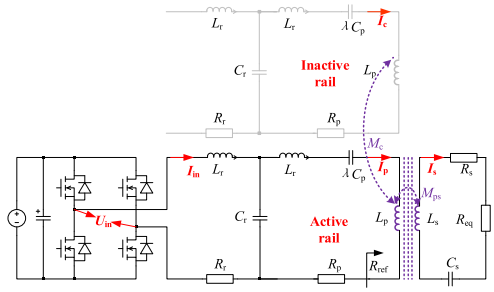

Fig. 2. Two PSRs system circuit.

PSRs, the self-inductance of each PSR is usually approximately equal, and is therefore assumed as $L_{p1} = L_{p2} = \ldots = L_{pn} = L_p$ throughout this article for simplicity. In this case, the compensation capacitors C_{pn} in Fig. 1 can be uniformly set to the same value, expressed as

$$C_{p1} = C_{p2} = \ldots = C_{pn} = \lambda C_p, n \in N^* \tag{6}$$

where λ is the resonance tuning coefficient, and C_p satisfies

$$C_p = \frac{1}{\omega^2 L_p}. \tag{7}$$

It can be seen that $\lambda = 1$ is a special case, corresponding to the CPCM. It is noted that when L_r and C_r remain resonant, changing the capacitor connected in series with the PSR does not alter the PSR current I_p, and the output voltage of the system also remains unchanged [28]. Therefore, the PPCM preserves the original system's constant-current and constant-voltage characteristics.

B. Analysis of ICC Characteristics

To quantitatively analyze the ICC, a two-PSR system as shown in Fig. 2, is considered, where one rail is active and the other is inactive. The AR current is denoted as I_p, the ICC in the IAR as I_c, the receiver current as I_s, and the cross-coupling MI as M_c. It is assumed that the secondary side is fully resonant, which can be expressed as

$$C_s = \frac{1}{\omega^2 L_s}. \tag{8}$$

By reflecting the load impedance to the primary side and neglecting the secondary side resistance R_s, the reflected impedance is given by

$$R_{ref} = \frac{(\omega Mps)^2}{R_{\text{eq}}} \tag{9}$$

where M_{ps} is the MI between the AR and receiver, and R_{eq} is the equivalent load resistance R_{Load} referred to the rectifier input, as shown in Fig. 1.

In this case, the system in Fig. 2 can be equivalently represented by the simplified model in Fig. 3, where variables with the subscript "eq" denote the corresponding equivalent values. The expressions and current conversion relationships are summarized in Table I.

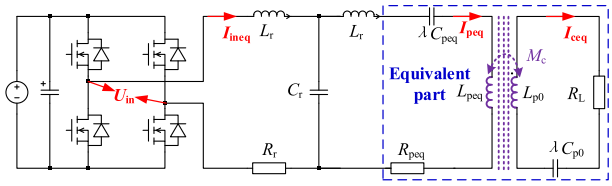

Fig. 3. Equivalent circuit of the two PSRs system.

TABLE I
VARIABLE CONVERSION RELATIONS

Variable	Conversion relationship	Variable	Conversion relationship
C_{peq}	C_p	R_L	R_p
L_{peq}	L_p	I_{ineq}	I_{in}
R_{peq}	$R_p+(\omega M_{ps})^2/R_{eq}$	I_{peq}	I_p
L_{p0}	L_p	I_s	$\omega M_{ps} I_{peq}/R_{eq}$
C_{p0}	C_p	I_{ceq}	I_c

By solving the circuit parameters in Fig. 3 and converting the results using Table I, the original circuit parameters of the two PSRs system in Fig. 2 can be obtained. Based on Kirchhoff's law, the equivalent circuit in Fig. 3 is modeled as follows:

$$\begin{bmatrix} j\omega L_r+\frac{1}{j\omega C_r}+R_r & -\frac{1}{j\omega C_r} & 0 \\ 0 & -j\omega M_c & j\omega L_{p0}+\frac{1}{j\omega\lambda C_{p0}}+R_L \\ -\frac{1}{j\omega C_r} & \xi & -j\omega M_c \end{bmatrix} \begin{bmatrix} I_{\text{ineq}} \\ I_{\text{peq}} \\ I_{\text{ceq}} \end{bmatrix} = \begin{bmatrix} U_{\text{in}} \\ 0 \\ 0 \end{bmatrix} \tag{10}$$

where ξ satisfies

$$\xi = j\omega L_r + j\omega L_{\text{peq}} + \frac{1}{j\omega\lambda C_{\text{peq}}} + \frac{1}{j\omega C_r} + R_{\text{peq}}. \tag{11}$$

By solving (10), I_{ineq} , I_{peq}, and I_{ceq} can be obtained as follows:

$$I_{\text{ineq}} = \frac{N_1}{D_1}\cdot U_{\text{in}} \tag{12}$$

$$I_{\text{peq}} = \frac{-j\lambda\omega L_r(\lambda(jR_L-\omega L_{p0})+\omega L_{p0})}{D_1}\cdot U_{\text{in}} \tag{13}$$

$$I_{\text{ceq}} = \frac{\lambda^2\omega^2 L_r M_c(\lambda(jR_L-\omega L_{p0})+\omega L_{p0})}{D_1(\lambda(j\omega L_{p0}+R_L)-j\omega L_{p0})}\cdot U_{\text{in}} \tag{14}$$

$$\begin{aligned} N_1 = {} & \lambda^2\left(j\omega^2(M_c{}^2-L_{p0}L_{\text{peq}})\right. \\ & \left.-\omega(L_{p0}R_{\text{peq}}+L_{\text{peq}}R_L)+jR_LR_{\text{peq}}\right) \\ & +\lambda\left(2j\omega^2 L_{p0}L_{\text{peq}}+\omega(L_{p0}R_{\text{peq}}+L_{\text{peq}}R_L)\right) \\ & -j\omega^2 L_{p0}L_{\text{peq}} \end{aligned} \tag{15}$$

$$\begin{aligned} D_1 = {} & \lambda^2\left(-\omega^3 L_{p0}L_r^2+j\omega^2\left(M_c{}^2R_r+L_r^2R_L-L_{p0}L_{\text{peq}}R_r\right)\right. \\ & \left.-\omega\left(L_{p0}R_{\text{peq}}+L_{\text{peq}}R_L\right)R_r+jR_LR_{\text{peq}}R_r\right) \\ & +\lambda\omega\left(L_{p0}R_{\text{peq}}+L_{\text{peq}}R_L\right)R_r \\ & +\lambda\left(\omega^3 L_{p0}L_r^2+2j\omega^2 L_{p0}L_{\text{peq}}R_r\right) \\ & -j\omega^2 L_{p0}L_{\text{peq}}R_r. \end{aligned} \tag{16}$$

TABLE II
SYSTEM INITIAL PARAMETERS

Variable	Value	Variable	Value
U_{in}	540 V	M_{ps}	30 μH
f	85 kHz	M_c	−0.7 μH
L_r	13 μH	R_r	0.02 Ω
L_p	150 μH	R_p	0.1 Ω
L_s	100 μH	R_{eq}	12.16 Ω

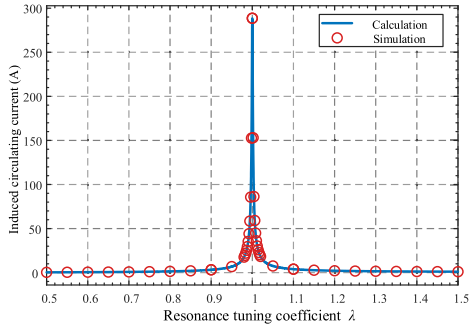

Fig. 4. Comparison between the calculated and simulated I_c.

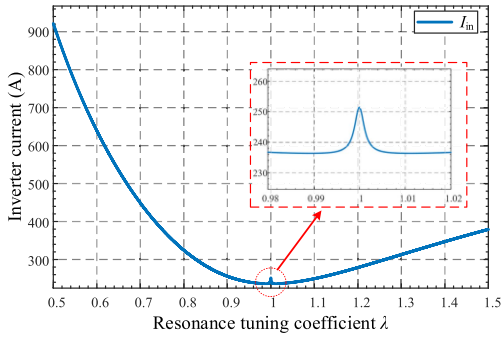

Fig. 5. Inverter current versus λ values.

To verify the accuracy of the proposed model, a set of basic system parameters is provided in Table II. To ensure consistency in the data analysis, all subsequent verification procedures are conducted based on the parameters in Table II. Taking different values of λ as examples, the calculated and simulated values of I_c are compared in Fig. 4. As shown in Fig. 4, the calculated and simulated values are very close, verifying the accuracy of the circuit modeling. With the increase of λ, the ICC first increases and then decreases, reaching its maximum at $\lambda = 1$. This indicates that the CPCM results in the largest ICC.

C. Abnormal Drop Characteristic of Inverter Current

The inverter current versus λ for the circuit in Fig. 2 and parameters in Table II is shown in Fig. 5. As λ deviates from 1, the current rises due to the additional reactive power introduced by detuning. However, a small dip appears near $\lambda = 1$, where some λ values yield lower inverter current than the CPCM ($\lambda = 1$). The observed drop in inverter current is unusual. To investigate

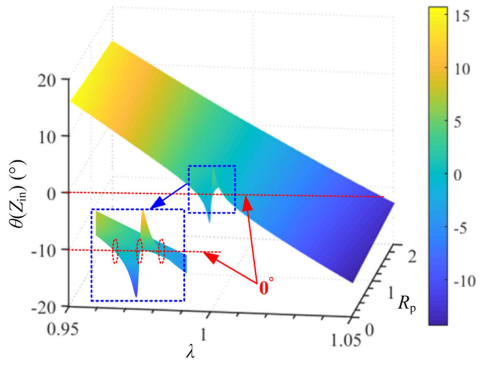

Fig. 6. Impedance angle $\theta(Z_{\text{in}})$ versus λ values.

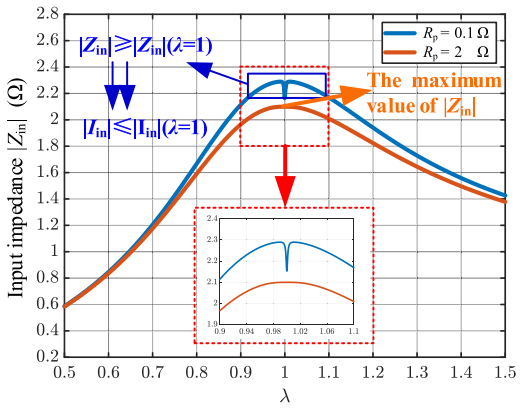

Fig. 7. Input impedance $|Z_{\text{in}}|$ versus λ values.

this, the impedance angle at the inverter input $\theta(Z_{\text{in}})$ ($Z_{\text{in}} = U_{\text{in}} / I_{\text{in}}$) is plotted in Fig. 6.

As shown in Fig. 6, when the resistance R_p of the IAR is small, $\theta(Z_{\text{in}})$ crosses the 0° line three times, indicating the presence of three resonance points. In contrast, when R_p is large, $\theta(Z_{\text{in}})$ exhibits only a single zero crossing, corresponding to a single resonance point. To assess whether other parameters in Fig. 2 affect the number of resonance points, a parameter sweep was performed by varying the horizontal axis variable in Fig. 6 while keeping all other parameters constant. The results show that as long as L_r and C_r , as well as L_s and C_s , remain in resonance, the value of R_p solely determines the number of resonance points. Specifically, when R_p is below 0.5 Ω, three resonance points consistently appear at the inverter input.

Note that R_p denotes the parasitic resistance of the PSR. In practical segmented rails DWPT systems, R_p is typically below 0.5 Ω [15], [29], indicating that three resonance points typically exist at the inverter input.

As shown in Fig. 6, when $R_p = 0.1$ Ω, three resonance points exist at the inverter input, while only one resonance point exists when $R_p = 2$ Ω. The magnitude of the inverter input impedance $|Z_{\text{in}}|$ versus λ for $R_p = 0.1$ Ω and $R_p = 2$ Ω is shown in Fig. 7.

As seen in Fig. 7, when there is only one resonance point at the inverter input, $|Z_{\text{in}}|$ peaks at $\lambda = 1$, resulting in the lowest inverter current. However, when three resonance points exist, several λ values lead to a higher $|Z_{\text{in}}|$ than at $\lambda = 1$, meaning the inverter current is even lower. Therefore, the observed drop in inverter current is attributed to the presence of multiple resonance points at the inverter input. These relationships can be summarized as

$$\begin{cases} \max\left(|Z_{\text{in1}}|, |Z_{\text{in0}}|, |Z_{\text{in2}}|\right) = |Z_{\text{in0}}| \\ \min\left(|I_{\text{in1}}|, |I_{\text{in1}}|, |I_{\text{in2}}|\right) = |I_{\text{in0}}| \end{cases} \tag{17}$$

where max and min denote the maximum and minimum functions, the subscript 0 corresponds to the natural resonance point ($\lambda = 1$), and the subscripts 1 and 2 correspond to the resonance points on the left and right sides of the natural resonance point, respectively.

TABLE III
COMPARISON OF SIMULATION PARAMETERS

Parameter	λ=1	λ=0.96
I_{in}	249.2 A	238.8 A
I_p	77.1 A	77.1 A
I_s	100.8 A	100.9 A
P_s	123.5 kW	123.5 kW
I_c	288.1 A	8.6 A
$\theta(Z_{\text{in}})$	1.8°	10.7°

D. Comparison of Circuit Parameters

Based on the analysis results from Figs. 4–6, when multiple resonance points exist, $\theta(Z_{\text{in}})$ tends to be capacitive on the right side of $\lambda = 1$, which is unfavorable for soft switching. On the left side of $\lambda = 1$, there may exist λ values that significantly reduce the ICC, lower the inverter current, and result in an inductive $\theta(Z_{\text{in}})$. Therefore, in this article, a parameter configuration with $\lambda < 1$ is adopted to achieve better system performance. For the parameters in Table II, a comparison of system simulation results at $\lambda = 1$ and $\lambda = 0.96$ is presented in Table III, where P_s is the output power.

As shown in Table III, compared with the CPCM, the PPCM significantly reduces ICC from 288.1 to 8.6 A while maintaining the same current of transmitter and output power. The inverter current and required capacity are also reduced. Although $\theta(Z_{\text{in}})$ increases slightly, the overall benefit is evident.

IV. Analysis of Multiple PSRs System

A. Analysis of ICC Diffusion Characteristics

To analyze the ICC in IARs, an equivalent circuit with multiple PSRs is established, as shown in Fig. 8. An example is considered in which all IARs are placed on the right side of the AR.

1) ICCs of CPCM: For the CPCM, the number of IARs is denoted as a, and all cross-coupling MI between rails set to M_c. According to the MI model and Kirchhoff's law, the ICCs in the right-side IARs satisfy the equations shown in (18).

$$\begin{pmatrix} R_p & -j\omega M_c & 0 & \cdots & 0 \\ -j\omega M_c & R_p & -j\omega M_c & \cdots & 0 \\ 0 & -j\omega M_c & R_p & \cdots & 0 \\ \vdots & \vdots & \vdots & \ddots & -j\omega M_c \\ 0 & 0 & 0 & -j\omega M_c & R_p \end{pmatrix}$$

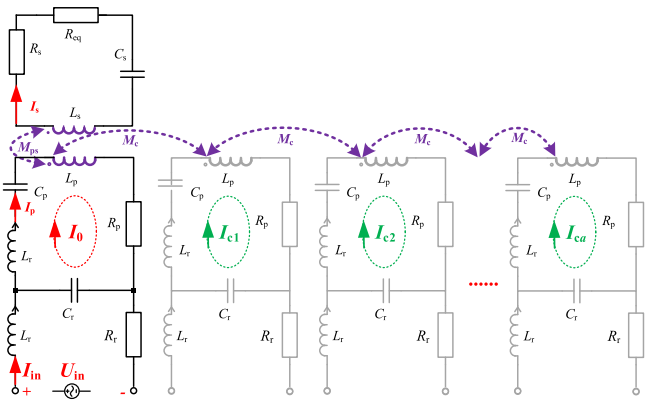

Fig. 8. Equivalent circuit model with IARs on the right side of the AR.

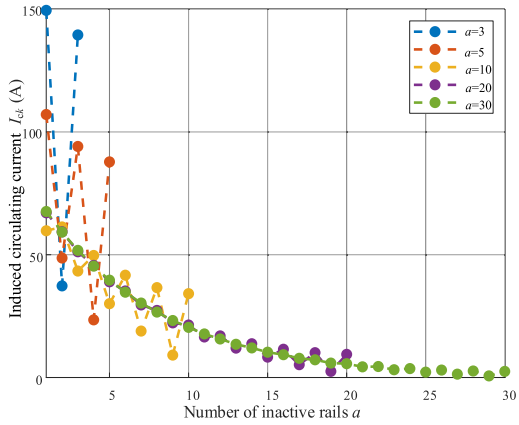

Fig. 9. Variation of ICCs with different numbers of IARs.

$$\begin{pmatrix} I_{c1} \\ I_{c2} \\ I_{c3} \\ \vdots \\ I_{ca} \end{pmatrix} = \begin{pmatrix} j\omega M_c I_0 \\ 0 \\ 0 \\ \vdots \\ 0 \end{pmatrix}. \tag{18}$$

For (18), when the number of IARs is fixed, the ICCs can be found by matrix inversion. However, this method does not show how cross-coupling MI affects the ICCs, or how the ICCs change with the number of IARs. Therefore, it is necessary to seek a general solution of (18).

Equation (18) can be regarded as a tridiagonal Toeplitz matrix, which is mathematically equivalent to a boundary-value problem of a second-order linear homogeneous difference equation. Accordingly, (18) is transformed into a homogeneous recurrence relation

$$R_p I_{ck} - j\omega M_c \left(I_{c(k-1)} + I_{c(k+1)}\right) = 0 \quad (k = 2, 3, \ldots, a-1). \tag{19}$$

Assuming a general solution of the form $I_{ck} = Ce^{\gamma}$ (C is a constant), substitution yields the characteristic equation

$$R_p - j\omega M_c \left(e^{-\gamma} + e^{\gamma}\right) = 0. \tag{20}$$

Using the definition of hyperbolic cosine, $\cosh(\gamma) = (e^{\gamma} + e^{-\gamma})/2$, (20) is simplified

$$R_p - 2j\omega M_c \cosh(\gamma) = 0. \tag{21}$$

The solution is obtained as $\gamma = \pm\theta$, θ is

$$\theta = \cosh^{-1}\left(\frac{R_p}{2j\omega M_c}\right) \tag{22}$$

where θ is the complex propagation constant of ICCs in IARs, determined by the rail resistance R_p, the cross-coupling MI M_c, and the angular frequency ω.

The general solution can be expressed as

$$I_{ck} = Ae^{\theta k} + Be^{-\theta k} \ (k = 1, 2, \ldots, a). \tag{23}$$

With boundary conditions applied, the closed-form solution of I_{ck} is derived

$$I_{ck} = I_0 \cdot \frac{\sinh\left((a+1-k)\theta\right)}{\sinh\left((a+1)\theta\right)}, \quad k, a \in N^*, \quad k \le a. \tag{24}$$

Equation (24) indicates that the ICCs follow a hyperbolic-sine distribution and progressively diffuse along the IARs. For the parameters in Table II and different numbers of IARs a, the corresponding I_{ck} values calculated using (24) are shown in Fig. 9.

As shown in Fig. 9, when the number of IARs is large, the ICC gradually decays to zero. However, with fewer IARs, the ICC propagates in a damped oscillatory manner. A smaller number of IARs result in stronger oscillations and higher overall ICC. Moreover, the ICC at the same rail position varies with a. For example, the third IAR has $I_{c3} = 139.51$ A when $a = 5$, and $I_{c3} = 94.08$ A when $a = 3$.

In actual applications, to improve efficiency and shorten the power busbars, fewer than ten PSRs are typically powered by one inverter. Thus, under the CPCM, ICCs in the IARs will persist. This behavior of ICC can be referred to as the diffusion characteristic, which physically represents the phenomenon in multiple PSRs DWPT system where the ICC generated in the AR is electromagnetically coupled into adjacent IARs, and then further propagated and attenuated toward farther IARs through the cross-coupling MIs.

The diffusion characteristic of the ICC increases system losses and inverter capacity, reduces efficiency, and affects system safety and lifetime. In practical applications, when the power level is low or the cross coupling between PSRs is weak, the ICC may be small and its impact can be approximately ignored. However, whether this influence can be ignored depends on the specific design objectives of the system. These objectives are usually defined by the designer. For example, in a system with multiple PSRs, the maximum ICC may be required to remain below one tenth of the current in the AR. In high power transmission, the maximum ICC may be required to remain below 10 A, or the loss on IARs may be required to remain below 0.1 percent of the output power. If the ICC becomes excessively large in practical applications, suppression measures must be taken.

The following section analyzes how the proposed method suppresses the diffusion characteristic of the ICC in multiple PSRs system.

2) ICCs of PPCM: When the proposed method is applied, the loop impedance of IAR changes from R_p to $R_p + j\omega L_p(1\text{-}1/\lambda)$.

According to (18)–(24), the corresponding general expression of the ICC can be written as

$$I_{ck} = I_0 \cdot \frac{\sinh\left((a+1-k)\theta_{\text{pro}}\right)}{\sinh\left((a+1)\theta_{\text{pro}}\right)}, \quad k, a \in N^*, \quad k \le a \tag{25}$$

where θ_{pro} is

$$\theta_{\text{pro}} = \cosh^{-1}\left(\frac{j\omega L_p(1-\frac{1}{\lambda}) + R_p}{2j\omega M_c}\right). \tag{26}$$

For a DWPT system with multiple PSRs, after neglecting the current in adjacent IARs, the current in the IAR closest to the AR can be obtained from (1) and (6) as

$$I_{c1} = \frac{-j\omega M_c I_p}{j\omega L_p(1-\frac{1}{\lambda}) + R_p}. \tag{27}$$

As described in Section III, in a system with two PSRs, the PPCM can effectively suppress the ICC in the IAR, meaning that the current in the IAR closest to the AR is greatly reduced. Therefore, in a system with multiple PSRs, the currents in the subsequent IARs are usually very small. As a result, I_{c1} corresponds to the maximum ICC under the PPCM for a given value of λ. The maximum value of (27), denoted as $I_{c1\_\max}$, is given by

$$I_{c1\_\max} = \frac{\omega M_c I_p}{R_p}. \tag{28}$$

$I_{c1\_\max}$ corresponds to the maximum ICC under the CPCM. To evaluate the suppression achieved by the PPCM relative to the maximum ICC of the CPCM, the attenuation coefficient of the ICC, α_{ICC}, is defined as

$$\alpha_{\text{ICC}} = \frac{|I_{c1}|}{I_{c1\_\max}} = \frac{R_p}{\sqrt{\omega^2 {L_p}^2 (1-\frac{1}{\lambda})^2 + {R_p}^2}}. \tag{29}$$

A smaller attenuation coefficient of the ICC indicates a better suppression effect. The quality factor of the PSR is $Q_{Lp} = \omega L_p / R_p$. Substituting this into (29) gives

$$\alpha_{\text{ICC}} = \frac{1}{\sqrt{{Q_{Lp}}^2 (1-\frac{1}{\lambda})^2 + 1}}. \tag{30}$$

Based on (30) the attenuation coefficient α_{ICC} corresponding to different quality factor of the PSR Q_{Lp} can be plotted as shown in Fig. 10.

In Fig. 10, when λ is fixed, a higher Q_{Lp} results in a smaller attenuation coefficient α_{ICC}, indicating a better suppression effect. Therefore, in practical systems, it is desirable to design with a larger L_p and a smaller R_p. In this case, the parameter λ only needs to be set near 1. When Q_{Lp} is small, however, λ should be set as far away from 1 as possible to achieve better suppression of the ICC.

Based on (24), (25), and the basic system parameters listed in Table II, the variation of the ICC under different parameter configuration methods can be plotted as shown in Fig. 11.

In Fig. 11, the ICC in the IARs persists when the CPCM is used. In contrast, with the PPCM, only the first IAR carries a noticeable current, while the ICCs in the subsequent IARs are almost zero. Therefore, the PPCM can effectively suppress the diffusion characteristic of the ICC.

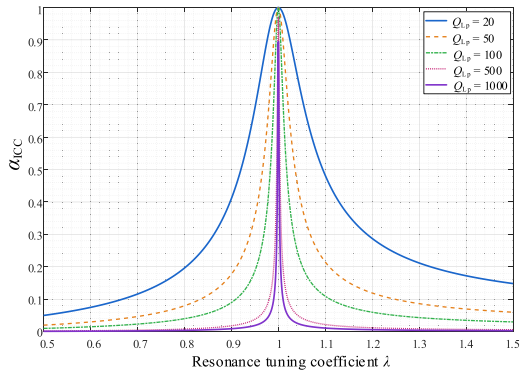

Fig. 10. Attenuation coefficient α_{ICC} of the ICC for different quality factors Q_{Lp}.

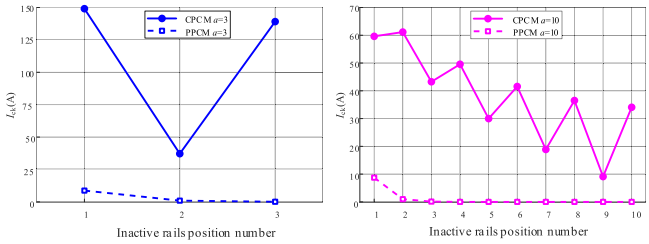

Fig. 11. Comparison of the diffusion characteristics of the ICC between the CPCM and the PPCM. (a) $a = 3$. (b) $a = 10$.

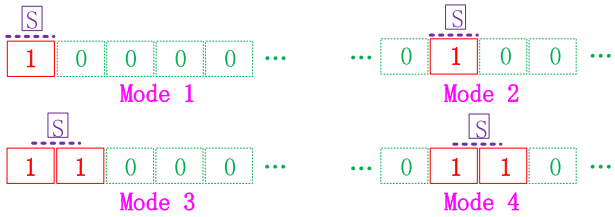

Fig. 12. Different operating modes.

B. General Circuit Analysis Model

When the receiver is in different positions, the operating mode of PSRs changes, leading to variations in the inverter current and ICC. Therefore, it is necessary to analyze how the circuit parameters vary with receiver position. For a single receiver, four typical operating modes can be summarized, as shown in Fig. 12, where "1" denotes an AR, "0" an IAR, and "S" the receiver.

Considering CPCM and PPCM, a total of eight operating modes need to be analyzed. To simplify the calculations, a general circuit analysis model is proposed to solve the circuit parameters for all eight operating modes.

First, based on Kirchhoff's law and impedance reflection relationships, the circuits under different operating modes are equivalently transformed into the general model shown in Fig. 3. The parameters of the "Equivalent part" in Fig. 3 vary depending on the operating mode, with the specific values summarized in Table IV.

TABLE IV
PARAMETER CORRESPONDENCE FOR THE EIGHT DIFFERENT OPERATING MODES

Mode	Mode1		Mode2		Mode3		Mode4	
–	Con	Pro	Con	Pro	Con	Pro	Con	Pro
C_{peq}	C_p	C_p	C_p	C_p	$C_p/2$	$C_p/2$	$C_p/2$	$C_p/2$
L_{peq}	L_p	L_p	L_p	L_p	$2L_p$	$2L_p$	$2L_p$	$2L_p$
R_{peq}	$\frac{(\omega M_{ps})^2}{R_{eq}}+R_p$	$\frac{(\omega M_{ps})^2}{R_{eq}}+R_p$	$\frac{(\omega M_{ps})^2}{R_{eq}}+R_p$	$\frac{(\omega M_{ps})^2}{R_{eq}}+R_p$	R_d	R_d	R_d	R_d
L_{p0}	L_p	L_p	$L_p/2$	$L_p/2$	L_p	L_p	$L_p/2$	$L_p/2$
C_{p0}	C_p	C_p	$2C_p$	$2C_p$	C_p	C_p	$2C_p$	$2C_p$
R_L	R_{LR}	R_p	$R_{LR}//R_{LL}$	$R_p/2$	R_{LR}	R_p	$R_{LR}//R_{LL}$	$R_p/2$
I_{in}	I_{ineq}	I_{ineq}	I_{ineq}	I_{ineq}	I_{ineq}	I_{ineq}	I_{ineq}	I_{ineq}
I_p	I_{peq}	I_{peq}	I_{peq}	I_{peq}	I_{peq}	I_{peq}	I_{peq}	I_{peq}
I_s	$\frac{\omega M_{ps} I_{peq}}{R_{eq}}$	$\frac{\omega M_{ps} I_{peq}}{R_{eq}}$	$\frac{\omega M_{ps} I_{peq}}{R_{eq}}$	$\frac{\omega M_{ps} I_{peq}}{R_{eq}}$	$\frac{(\omega M_{pls}+\omega M_{prs})I_{peq}}{R_{eq}}$	$\frac{(\omega M_{pls}+\omega M_{prs})I_{peq}}{R_{eq}}$	$\frac{(\omega M_{pls}+\omega M_{prs})I_{peq}}{R_{eq}}$	$\frac{(\omega M_{pls}+\omega M_{prs})I_{peq}}{R_{eq}}$
I_c	*ex*	I_{ceq}	*ex*	$I_{ceq}/2$	*ex*	I_{ceq}	*ex*	$I_{ceq}/2$

TABLE V
COMPARISON OF SIMULATED AND CALCULATED VALUES

Mode	Calculation value (A)				Simulation value (A)			
	I_{cmax_Con}	I_{cmax_Pro}	I_{in_Con}	I_{in_Pro}	I_{cmax_Con}	I_{cmax_Pro}	I_{in_Con}	I_{in_Pro}
100 (Mode 1)	72.1	11.7	235.5	237.5	72.0	11.9	234.8	236.9
010 (Mode 2)	288.4	11.7	266.7	237.5	288.0	11.6	264.5	236.8
110 (Mode 3)	288.6	11.6	252.6	245.3	289.0	11.7	251.4	245.6
1000 (Mode 1)	149.1	11.7	243.5	237.5	149.1	11.9	241.7	236.9
0100 (Mode 2)	288.6	11.7	251.4	237.5	288.1	11.9	250.2	236.8
1100 (Mode 3)	72.1	11.7	237.5	245.3	72.4	12.0	237.0	245.6
0110 (Mode 4)	288.6	11.7	267.0	245.2	289.0	11.7	266.9	245.4

Next, using the KVL equation given in (10), I_{ineq}, I_{peq}, and I_{ceq} can be calculated as shown in (12)–(16).

Finally, the actual values of I_{in}, I_p, I_s, and I_c for each operating mode can then be derived from I_{ineq}, I_{peq}, and I_{ceq} through conversion. The conversion relationships are also summarized in Table IV, where "Con" denotes the conventional method and "Pro" denotes the proposed method.

In Table IV, M_{pls} and M_{prs} represent the MI between the receiver and the adjacent left and right ARs, respectively. "*ex*" indicates that the ICCs in the left and right IARs need to be expanded and calculated using (24). R_d is the total equivalent resistance reflected to the primary side when two PSRs are active. R_{LL} and R_{LR} are the left and right IAR resistances reflected to the nearest AR under the CPCM, given by (31) and (32), respectively

$$R_d = 2R_p + (\omega M_{pls} + \omega M_{prs})^2 / R_{eq} - 2j\omega M_c \tag{31}$$

$$\begin{cases} R_{LL} = R_p - j\omega M_c \frac{\sinh((a_L-1)\theta)}{\sinh(a_L\theta)} \\ R_{LR} = R_p - j\omega M_c \frac{\sinh((a_R-1)\theta)}{\sinh(a_R\theta)} \end{cases} \tag{32}$$

where a_L and a_R represent the numbers of IARs on the left and right sides of AR, respectively. θ is calculated according to (22).

In summary, for each operating mode shown in Fig. 12, the corresponding inverter current, ICC, and load current can be obtained by substituting the equivalent circuit parameters from Table IV into (12)–(16) and (24).

To verify the accuracy of the proposed general circuit analysis model, simulation is performed for systems with three and four PSRs. For simplicity, it is assumed that the total MI (M_{pls} + M_{prs}) in the two-AR operating mode is equal to the MI (M_{ps}) in the single-AR operating mode. The system parameters are consistent with those in Table II. The inverter current and the maximum ICC under different modes are summarized in Table V. $\lambda = 0.97$ is used for the proposed method.

As shown in Table V, the simulated and calculated values of the inverter current and ICC closely match, validating the accuracy of the proposed general analysis model and the parameter relationships summarized in Table IV for various PSR operating modes. Furthermore, compared with the CPCM, the PPCM significantly reduces the peak ICC from 289 to 11.7 A and maintains stable peak values around 11.9 A across different operating modes.

C. Design Method of λ

The main differences between CPCM and PPCM are inverter capacity, ICC, system efficiency (dc–dc efficiency), and inverter input impedance angle. The system efficiency η_{dc-dc} is calculated by

$$\eta_{DC--DC} = \eta_{inv} \cdot \frac{{I_s}^2 \cdot R_{eq}}{\sum_{j=1}^{j=\alpha} {I_{inj}}^2 \cdot R_r + {I_p}^2 \cdot R_p + {I_s}^2 \cdot R_{eq} + \sum_{k=1}^{k=\beta} {I_{ck}}^2 \cdot R_p} \cdot \eta_{rec} \tag{33}$$

where η_{inv} and η_{rec} are the efficiencies of the inverter and rectifier, respectively; α is the number of ARs ($\alpha = 1$ or 2); β is the number of IARs ($\beta \in N^*$); and I_{ck} is ICC in the kth IAR.

For CPCM and PPCM, I_p and I_s are the same, so the rectifier efficiency is identical. Assuming the inverter efficiency remains

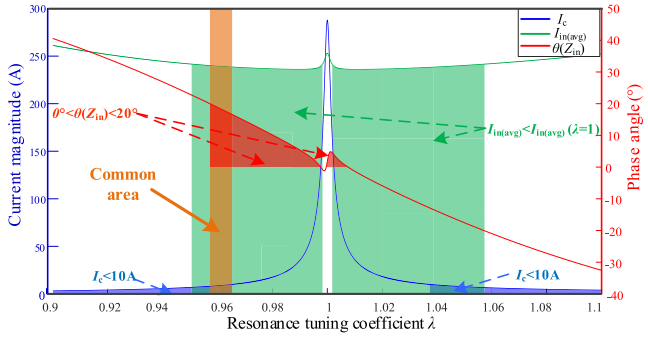

Fig. 13. Three metrics versus λ values.

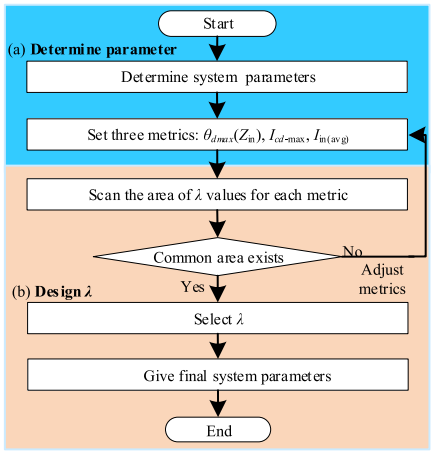

Fig. 14. Design flowchart of the resonance tuning coefficient λ.

constant under high-power output, the efficiency difference between the two methods lies in

$$\sum_{j=1}^{j=\alpha} {I_{\mathrm{in}j}}^2 \cdot R_r + \sum_{k=1}^{k=\beta} {I_{ck}}^2 \cdot R_p. \tag{34}$$

It can be seen that the system efficiency is mainly affected by the inverter current and ICC. Therefore, I_{in}, I_c, and $\theta(Z_{\mathrm{in}})$ are used to evaluate the performance of PPCM. As shown in Table V, I_{in} varies under different operating modes. Considering the entire operating process, the average I_{in} is defined as

$$I_{\mathrm{in(avg)}} = \frac{\int I_{\mathrm{in}(i)} \cdot t_{(i)}}{t_{(1)} + t_{(2)} + t_{(3)} + t_{(4)}}, i = 1, 2, 3, 4 \tag{35}$$

where $I_{\mathrm{in}(i)}$ and $t_{(i)}$ are the inverter current and operating time for the ith operating mode.

To simplify system parameter design, it is assumed that the system operates for a duration t in each single-AR mode and for εt in each two-AR mode. Considering that the transition time is relatively short, ε is set to 0.2 in this article.

A design example is provided for a four-PSR system, with parameters consistent with those in Table II. Based on Table V and (35), the average inverter current under the CPCM is 246.1 A. Assuming the target maximum ICC ($I_{cd\text{-max}}$) is 10 A and the maximum inverter input impedance angle $\theta_{d\text{-max}}(Z_{\mathrm{in}})$ is 20°. The corresponding curves of $\theta_{d\text{-max}}(Z_{\mathrm{in}})$, $I_{cd\text{-max}}$, and $I_{\mathrm{in(avg)}}$ versus λ are shown in Fig. 13.

According to Fig. 13, λ values in the range of 0.9572 to 0.9653 satisfy all three design criteria. As λ increases, the inverter input impedance angle $\theta(Z_{\mathrm{in}})$ and inverter capacity decreases, Conversely, decreasing λ results in a lower ICC, which helps reduce unnecessary losses in IARs. Considering the tradeoff between these factors, a value of $\lambda = 0.96$ is selected as a balanced choice. Since this value lies within the common feasible region, both the inverter current and the ICC remain lower than those obtained with the CPCM. Furthermore, as indicated by indicated by (34), the PPCM also achieves higher system efficiency.

Based on the above-mentioned design procedure, the overall design flowchart is summarized in Fig. 14.

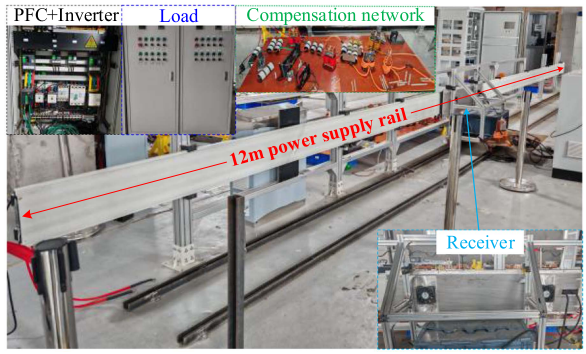

Fig. 15. Experimental platform.

V. Experimental Verification

A. Experimental Prototype

To verify the effectiveness of the PPCM, experimental validation was first carried out using a two-PSR system as shown in Fig. 2. The experimental setup for the DWPT system of port transportation equipment is presented in Fig. 15. Since different types of magnetic couplers can all be represented using the self-inductance and MI parameters shown in Fig. 1, the analytical method proposed in this paper is universally applicable to various magnetic couplers. Therefore, a simple unipolar PSR was adopted in this article [5].

The length of PSR is 12 m, with a spacing of 20 mm. The receiver length is 1.2 m, and the transmission gap is 30 mm. The inverter frequency is 85 kHz. Other detailed parameters are listed in Table VI. By calculation, $I_{\mathrm{in(avg)}} = 156.6$ A is obtained, with $\theta_{d\text{-max}}(Z_{\mathrm{in}}) = 20°$ and $I_{cd\text{-max}} = 10$ A set. Substituting the measured system parameters into the design flowchart in Fig. 12 yields a feasible λ range of 0.965–0.972, from which $\lambda = 0.97$ is chosen for the experiment.

To verify the characteristic of multiple resonance points in the inverter input impedance, the impedance analyzer (Keysight E4990A) was used to measure the frequency response of the impedance angle shown in Fig. 16. The measurement was taken

TABLE VI
EXPERIMENTAL PLATFORM PARAMETERS

Variable	Value	Variable	Value
L_{r1}	13.33 μH	C_{r1}	263.1 nF
L_{r2}	13.45 μH	C_{r2}	261.5 nF
L_{p1}	160.3 μH	$C_{p1(\lambda=1)}$	23.31 nF
L_{p2}	158.6 μH	$C_{p2(\lambda=1)}$	23.61 nF
L_s	93.65 μH	$C_{p1(\lambda=0.97)}$	22.88 nF
M_{ps}	25.16 μH	$C_{p2(\lambda=0.97)}$	22.63 nF
M_c	−0.73 μH	C_s	37.42 nF
R_{r1}	0.152 Ω	R_{p1}	0.147 Ω
R_{r2}	0.167 Ω	R_{p2}	0.138 Ω
R_s	0.88 Ω	R	15.2 Ω

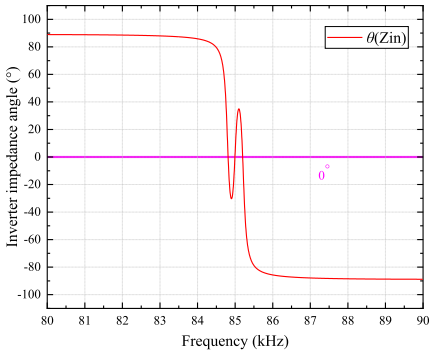

Fig. 16. Inverter input impedance angle versus frequency.

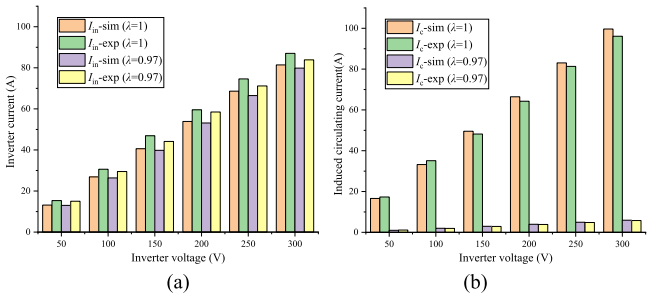

Fig. 17. Comparison of simulated and measured parameters for different λ values. (a) Inverter current. (b) ICC.

with the receiver open-circuited and the initial parameter set to λ = 1. It can be observed that the measured input impedance angle of the inverter has three zero-crossing points, corresponding to frequencies of approximately 84.8, 85, and 85.2 kHz. According to (12), the real and imaginary parts of the inverter input impedance can be altered by adjusting the parameter λ, which in turn causes shifts in the resonance frequencies. This verifies the multiresonance point characteristic of the proposed system.

B. Comparison of the Configuration Methods

To verify the ICC suppression effect of the proposed method, the inverter current and ICC under λ = 1 and λ = 0.97 were compared. The results are shown in Fig. 17.

As shown in Fig. 17(a), the simulated and measured inverter currents agree well. The inverter current under PPCM (λ = 0.97) is consistently lower than that under CPCM (λ = 1),

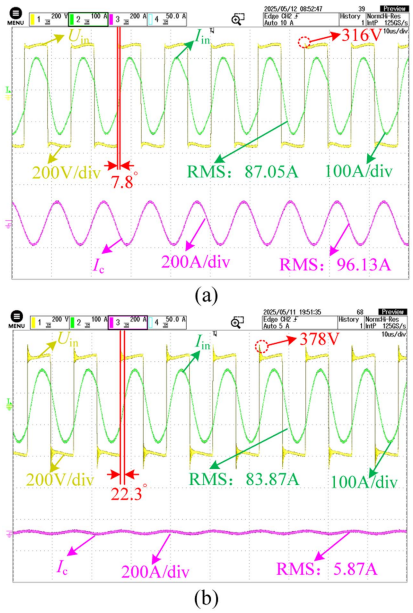

Fig. 18. Circuit response waveforms. (a) λ = 1. (b) λ = 0.97.

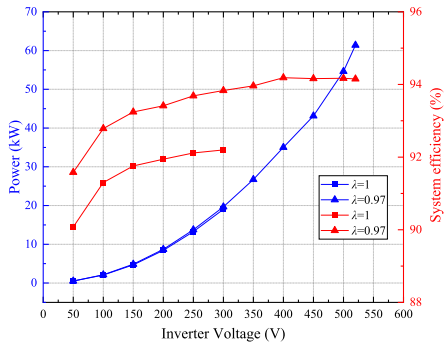

Fig. 19. Power and efficiency comparison.

indicating that the PPCM effectively reduces the inverter current and capacity. Fig. 17(b) shows that the simulated and measured ICCs are also close. The PPCM significantly reduces ICC. For example, when the inverter voltage is 300 V, the measured ICC is 96.13 A under the CPCM, while it is only 5.87 A under the PPCM. In this case, the ICC of CPCM is too high for the PSR to operate continuously. A comparison of circuit responses at 300 V inverter voltage for both configurations is shown in Fig. 18.

As shown in Fig. 18, the PPCM still significantly reduces ICC. Moreover, compared with the CPCM, the inverter current decreases from 87.05 to 83.87 A under the PPCM. However, a slightly larger input impedance angle is observed, with the inverter voltage peak rising from 316 to 378 V.

The load power and system's dc–dc efficiency curves for the two parameter configuration methods are shown in Fig. 19. As presented in Fig. 19, when the inverter voltage is 300 V, both parameter configuration methods achieve an output power of approximately 19.6 kW. However, the PPCM improves the system efficiency from 92.16% to 93.83%. According to (34),

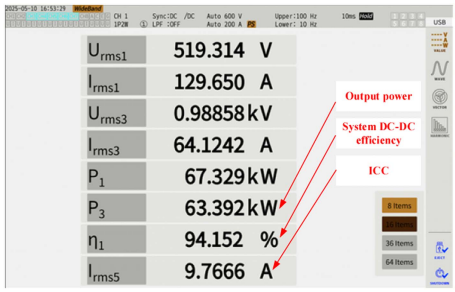

Fig. 20. Screenshot of the power analyzer.

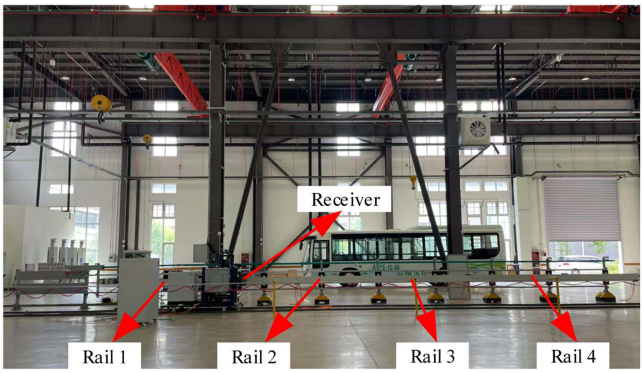

Fig. 21. Experimental platform with four PSRs.

this improvement mainly results from the reduced ICC and inverter current.

In summary, the PPCM not only significantly reduces ICC but also lowers the inverter current and capacity while improving the overall system efficiency. The maximum output power, peak system efficiency, and ICC achieved using the PPCM are shown in Fig. 20.

As depicted in Fig. 20, the PPCM achieves a maximum output power of 63.39 kW, a peak efficiency of 94.15%, and a maximum ICC of only 9.76 A.

C. Verification of ICC Diffusion Characteristics and General Circuit Analysis Model

To verify the diffusion characteristic of ICC, a 24-m test platform with four PSRs was built, as shown in Fig. 21.

The ICC parameters for $\lambda = 1$ and $\lambda = 0.97$ under Mode 1 operation (see Fig. 12) with an inverter output voltage of 300 V are shown in Fig. 22 for comparison.

As demonstrated in Fig. 22, the CPCM and the PPCM achieve similar output power, while the proposed method provides higher system efficiency and lower inverter current. In addition, under the CPCM, ICC (I_{c1}, I_{c2}, and I_{c3}) persists along IARs, confirming its diffusion characteristic. In contrast, the PPCM effectively suppresses ICC, making it negligible in subsequent rails. These results demonstrate the effectiveness of the PPCM in limiting ICC diffusion.

The accuracy of the general circuit analysis model was verified by comparing the maximum ICC, inverter current, and

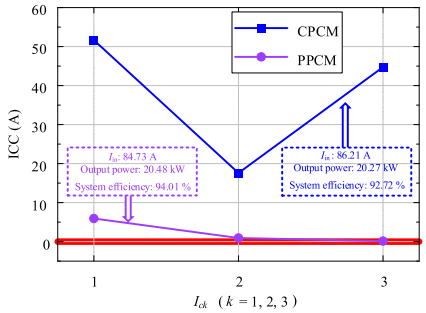

Fig. 22. Verification of the diffusion characteristic of the ICC.

TABLE VII
COMPARISON OF CALCULATED AND EXPERIMENTAL VALUES UNDER DIFFERENT OPERATING MODES

Mode	Mode1	Mode2	Mode3	Mode4
I_{cmax}-cal	6.04 A	6.04 A	6.04 A	6.04 A
I_{cmax}-exp	5.93 A	5.72 A	5.88 A	6.33 A
I_{in}-cal	79.78 A	79.77 A	79.17 A	79.15 A
I_{in}-exp	84.73 A	85.41 A	83.68 A	82.33 A
P_{out}-cal	20.32 kW	20.32 kW	18.89 kW	18.89 kW
P_{out}-exp	20.48 kW	20.63 kW	19.27 kW	19.04 kW

output power under different operating modes between the calculated and experimental results. The comparison is presented in Table VII, where "cal" denotes the calculated values from Table IV and "exp" denotes the experimental values.

According to Table VII, good agreement is observed between the maximum ICC and output power calculated by the proposed general circuit analysis model and the experimental results. Although slight deviations appear in the calculated inverter current, the overall values remain close. Therefore, the proposed general circuit analysis model can accurately predict the ICC, inverter current, and output power.

D. Verification of DWPT

When the receiver reaches the end of the first PSR, the second PSR is activated. Under the PPCM, the inverter voltage and current during the transition from the first to the second PSR are shown in Fig. 23. Fig. 23(a) presents the waveforms of the inverter voltage U_{in} and the total inverter current I_{in}, while Fig. 23(b) shows the waveforms of the inverter voltage U_{in} together with the inverter current of the first PSR (I_{in1}) and the inverter current of the second PSR (I_{in2}).

From Fig. 23(a), it is observed that when the receiver transitions from the first PSR to the second PSR, the inverter current exhibits only minor fluctuations, with values of 18.39 A before switching and 18.87 A after switching. Fig. 23(b) shows that during the transition, the inverter current of the first PSR decreases gradually while that of the second PSR increases. A magnified view further confirms stable operation, as the inverter currents before and after switching remain close, at 16.87 and 17.47 A, respectively. These results demonstrate that the system maintains stable inverter current and ensures good parameter stability during dynamic transitions.

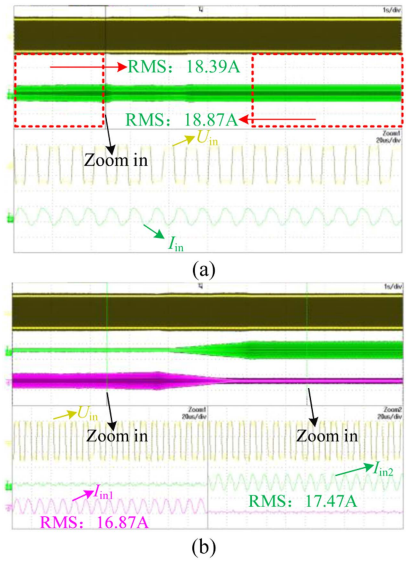

Fig. 23. Circuit waveforms during dynamic transition. (a) $U_{\rm in}$ and $I_{\rm in}$. (b) $U_{\rm in}$, $I_{\rm in1}$, and $I_{\rm in2}$.

VI. Conclusion

A parameter configuration method based on the resonance tuning coefficient λ has been proposed for the suppression of ICC in segmented-rail DWPT systems. It effectively reduces ICC without compromising output power or increasing system cost, while also lowering inverter capacity and improving efficiency. An abnormal drop in inverter current was observed during λ tuning. Analysis revealed that this phenomenon results from the presence of multiple resonance points at the inverter input. In systems with multiple PSRs, the conventional method causes a hyperbolic-sine-type diffusion of ICC, whereas the proposed method effectively suppresses it. A general circuit analysis model was developed for eight rail operating modes. Circuit parameter expressions were derived and summarized for various operating modes, which simplifies modeling and improves engineering applicability. Based on the general circuit analysis model, a parameter design method for the resonance tuning coefficient λ is presented.

Experimental results on a 12-m DWPT platform show that at 63.39 kW output, the ICC is 9.76 A and efficiency reaches 94.15%. At 19.6 kW output, the proposed method improves efficiency from 92.16% to 93.83%, lowers inverter current from 87.05 to 83.87 A, and reduces ICC from 96.13 to 5.87 A compared with the conventional method, confirming its effectiveness and performance advantages. To verify the diffusion characteristics of ICCs and the accuracy of the general circuit analysis model, an experimental platform consisting of four rails with a total length of 24 m was built. The experimental results show that the proposed method effectively suppresses the diffusion of ICCs, and the proposed general circuit analysis model can accurately calculate the ICC, inverter current, and output power.

References

[1] M. Behnamfar, T. O. Olowu, M. Tariq, and A. Sarwat, "Comprehensive review on power pulsation in dynamic wireless charging of electric vehicles," *IEEE Access*, vol. 12, pp. 66858–66882, 2024.

[2] C. C. Mi, G. Buja, S. Y. Choi, and C. T. Rim, "Modern advances in wireless power transfer systems for roadway powered electric vehicles," *IEEE Trans. Ind. Electron.*, vol. 63, no. 10, pp. 6533–6545, Oct. 2016.

[3] A. C. Bagchi, A. Kamineni, R. A. Zane, and R. Carlson, "Review and comparative analysis of topologies and control methods in dynamic wireless charging of electric vehicles," *IEEE J. Emerg. Sel. Top. Power Electron.*, vol. 9, no. 4, pp. 4947–4962, Apr. 2021.

[4] X. Li, C. Wang, H. Wang, X. Dai, Y. Sun, and A. P. Hu, "A robust wireless power transfer system with self-alignment capability and controllable output current for automatic-guided vehicles," *IEEE Trans. Power Electron.*, vol. 38, no. 10, pp. 11898–11906, Oct. 2023.

[5] E. S. Lee, M. Y. Kim, S. M. Kang, and S. H. Han, "Segmented IPT coil design for continuous multiple charging of an electrified monorail system," *IEEE Trans. Power Electron.*, vol. 37, no. 3, pp. 3636–3649, Mar. 2022.

[6] A. Zaheer, G. A. Covic, and D. Kacprzak, "A bipolar pad in a 10-kHz 300-W distributed IPT system for AGV applications," *IEEE Trans. Ind. Electron.*, vol. 61, no. 7, pp. 3288–3301, Jul. 2014.

[7] J. Huh, S. W. Lee, W. Y. Lee, G. H. Cho, and C. T. Rim, "Narrow-width inductive power transfer system for online electrical vehicles," *IEEE Trans. Power Electron.*, vol. 26, no. 12, pp. 3666–3679, Dec. 2011.

[8] Y. Yin, X. Gao, S. Dong, Y. Gao, N. Ding, and C. Zhu, "A high mass power density staggered U and I shaped pickup for dynamic wireless power transfer in rail transportation," *IEEE Trans. Ind. Electron.*, vol. 72, no. 9, pp. 9039–9049, Sep. 2025.

[9] C. Cai, M. Saeedifard, J. Wang, P. Zhang, J. Zhao, and Y. Hong, "A cost-effective segmented dynamic wireless charging system with stable efficiency and output power," *IEEE Trans. Power Electron.*, vol. 37, no. 7, pp. 8682–8700, Jul. 2022.

[10] Y. Li et al., "A new coil structure and its optimization design with constant output voltage and constant output current for electric vehicle dynamic wireless charging," *IEEE Trans. Ind. Informat.*, vol. 15, no. 9, pp. 5244–5256, Sep. 2019.

[11] J. Yin, S. Mekhilef, P. Darvish, H. Mokhlis, and T. K. Soon, "A new cross-overlapped decoupling coil structure for EV dynamic inductive wireless charging system," *IEEE Trans. Ind. Electron.*, vol. 72, no. 2, pp. 1314–1324, Feb. 2025.

[12] M. Yang, Y. Li, R. Mai, Z. He, and B. Wang, "Determining coil distance of cross-segmented IPT system for constant output voltage," in *Proc. IEEE Appl. Power Electron. Conf. Expo.*, 2017, pp. 1401–1406.

[13] K. Shi, C. Tang, H. Long, X. Lv, Z. Wang, and X. Li, "Power fluctuation suppression method for EV dynamic wireless charging system based on integrated magnetic coupler," *IEEE Trans. Power Electron.*, vol. 37, no. 1, pp. 1118–1131, Jan. 2022.

[14] G. Lee, M. Y. Kim, S. Lee, and J. H. Kim, "Operational verification of semi-dynamic wireless power transfer in light-rail transit systems," *IEEE Trans. Transp. Electrif.*, vol. 11, no. 1, pp. 348–358, Feb. 2025.

[15] J. H. Kim et al., "Development of 1-MW inductive power transfer system for a high-speed train," *IEEE Trans. Ind. Electron.*, vol. 62, no. 10, pp. 6242–6250, Oct. 2015.

[16] P. Sun, L. Wang, Y. Liang, X. Wu, and Q. Deng, "Analysis and cross-coupling elimination of input-series output-parallel (ISOP) multi-channel IPT system," *IEEE Open J. Power Electron.*, vol. 5, pp. 1014–1029, 2024.

[17] P. Jayathurathnage, Y. Liu, and J. Kyyra, "Self-decoupled and integrated coils for modular multitransmitter wireless power transfer systems," *IEEE Trans. Power Electron.*, vol. 37, no. 11, pp. 12962–12967, Nov. 2022.

[18] S. Zhou, C. Zhu, L. Zheng, S. Cui, and C. C. Chan, "Applying LCC compensated primary topology utilizing switches for transmitters with inter-coupling in a wireless power transmission system," *IEEE Access*, vol. 10, pp. 68257–68265, 2022.

[19] Y. Liu, R. Mai, D. Liu, Y. Li, and Z. He, "Efficiency optimization for wireless dynamic charging system with overlapped DD coil arrays," *IEEE Trans. Power Electron.*, vol. 33, no. 4, pp. 2832–2846, Apr. 2018.

[20] H. Wang and K. W. E. Cheng, "Analysis, design, and validation of a decoupled double-receiver wireless power transfer system with constant voltage outputs for industrial power supplies," *IEEE Trans. Ind. Informat.*, vol. 19, no. 1, pp. 362–370, Jan. 2023.

[21] A. Hossain, P. Darvish, S. Mekhilef, K. S. Tey, and C. W. Tong, "A new coil structure of dual transmitters and dual receivers with integrated decoupling coils for increasing power transfer and misalignment tolerance of wireless EV charging system," *IEEE Trans. Ind. Electron.*, vol. 69, no. 8, pp. 7869–7878, Aug. 2022.

[22] X. Li, J. Hu, H. Wang, X. Dai, and Y. Sun, "A new coupling structure and position detection method for segmented control dynamic wireless power transfer systems," *IEEE Trans. Power Electron.*, vol. 35, no. 7, pp. 6741–6745, Jul. 2020.

[23] F. Farajizadeh, D. M. Vilathgamuwa, D. Jovanovic, P. Jayathurathnage, G. Ledwich, and U. Madawala, "Expandable N-legged converter to drive closely spaced multitransmitter wireless power transfer systems for dynamic charging," *IEEE Trans. Power Electron.*, vol. 35, no. 4, pp. 3794–3806, Apr. 2020.
[24] H. Liu, L. Tan, X. Huang, M. Zhang, Z. Zhang, and J. Li, "Power stabilization based on switching control of segmented transmitting coils for multi loads in static-dynamic hybrid wireless charging system at traffic lights," *Energies*, vol. 12, no. 4, Apr. 2019, Art. no. 607.
[25] X. Gao, S. Dong, Y. Yin, Y. Zhang, and S. Cui, "An economical DWPT system with mutual compensation of segmented power supply rails based on LCL topology," *IEEE Trans. Transp. Electrif.*, vol. 9, no. 2, pp. 2865–2877, Jun. 2023.
[26] J. Zhang, X. Yuan, C. Wang, and Y. He, "Comparative analysis of two-coil and three-coil structures for wireless power transfer," *IEEE Trans. Power Electron.*, vol. 32, no. 1, pp. 341–352, Jan. 2017.
[27] W. Li, G. Wei, C. Cui, X. Zhang, and Q. Zhang, "A double-side self-tuning LCC/S system using a variable switched capacitor based on parameter recognition," *IEEE Trans. Power Electron.*, vol. 68, no. 4, pp. 3069–3078, Apr. 2021.
[28] W. Zhang and C. C. Mi, "Compensation topologies of high-power wireless power transfer systems," *IEEE Trans. Veh. Technol.*, vol. 65, no. 6, pp. 4768–4778, Jun. 2016.
[29] Y. Jiang, K. Chen, Z. Zhao, L. Yuan, T. Tan, and Q. Lin, "Designing an M-shape magnetic coupler for the wireless charging system in railway applications," *IEEE Trans. Power Electron.*, vol. 37, no. 1, pp. 1059–1073, Jan. 2022.

Yongping Yin received the M.E. degree in electrical engineering, from Harbin Institute of Technology (HIT), Harbin, China, in 2021, where he is currently working toward the Ph.D. degree in electrical engineering with the School of Electrical Engineering and Automation.

His research interest focuses on dynamic wireless power transfer.

Guangyao Li (Member, IEEE) received the B.S. and M.S. degrees in measurement and control technology and control engineering from Qingdao University of Science and Technology, Qingdao, China, in 2017 and 2020, respectively, and the Ph.D. degree in electrical engineering from Chonnam National University, Gwangju, South Korea, in 2024.

He is currently a Postdoctoral Associate Researcher with the Zhengzhou Research Institute, Harbin Institute of Technology (HIT), China. His research interests include dynamic wireless charging for electric vehicles and novel magnetic coupler modeling.

Xin Gao (Member, IEEE) was born in Shanxi Province, China. He received the B.S., M.S., and Ph.D. degrees in electrical engineering from the School of Electrical Engineering and Automation, Harbin Institute of Technology, Harbin, China, in 2016, 2018, and 2023, respectively.

He is currently a Lecturer with the School of Electrical Engineering and Automation, Harbin Institute of Technology, where he also works as a Postdoctoral Researcher. His research interests include wireless power transfer and power electronic converters.

Chang Liu was born in Heilongjiang Province, China. He received the B.S. degree in electrical engineering from the School of Electrical Engineering and Automation, Shandong University, Jinan, China, in 2021, and the M.S. degree in electrical engineering from the School of Electrical Engineering and Automation, Harbin Institute of Technology (HIT), Harbin, China, in 2023, where he is currently working toward the Ph.D. degree in electrical engineering.

His research interest focuses on wireless power transfer technology for electric vehicles.

Shuai Dong received the M.S. and Ph.D. degrees in electrical engineering from Harbin Institute of Technology (HIT), Harbin, China, in 2011 and 2016, respectively.

From 2017, he joined the Institute of Wireless Power Transfer Technology, HIT, where he is currently an Associate Professor.

His research interests include dynamic wireless power transfer technology and Z-Source converters

Chunbo Zhu received the M.E. and Ph.D. degrees in electrical engineering from the Harbin Institute of Technology (HIT), Harbin, China, in 1992 and 2001, respectively.

He is currently a Professor with the School of Electrical engineering and Automation, HIT, where he leads the Laboratory of Wireless Power Transfer and Battery Management Technologies. His current research interests include energy management systems, electric and hybrid electric vehicles, and wireless power transfer technologies.